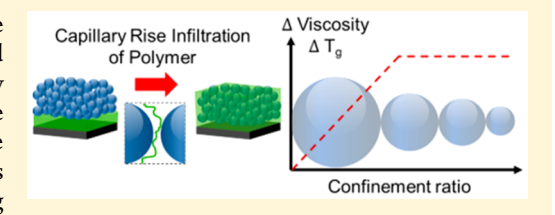
Effect of Physical Nanoconfinement on the Viscosity of Unentangled **Polymers during Capillary Rise Infiltration**

Jyo Lyn Hor,[†] Haonan Wang,[‡] Zahra Fakhraai,*,[‡] and Daeyeon Lee*,[†]

[†]Department of Chemical and Biomolecular Engineering and [‡]Department of Chemistry, University of Pennsylvania, Philadelphia, Pennsylvania 19104, United States

Supporting Information

ABSTRACT: We investigate the role of physical confinement on the polymer viscosity and the glass transition temperature (T_o) of unentangled polymers undergoing capillary rise infiltration (CaRI). CaRI thermally drives polymer infiltration into the voids of densely packed nanoparticle films via capillarity, inducing extreme nanoconfinement of the polymer. We tune the confinement ratio (CR), defined as the ratio of the polymer radius of gyration to the average pore radius in the nanoparticle packing, by using different polymer molecular weights and by varying the nanoparticle size



constituting the packing, respectively. We show that physical confinement of unentangled polymers in the interstices of weakly interacting nanoparticles leads to increased viscosity by more than 2 orders of magnitude relative to the bulk viscosity and to increased polymer $T_{\rm g}$ by 32 K. The increase in both viscosity and $T_{\rm g}$ increases with CR and saturates at CR \sim 1. The correlation between the viscosity and $T_{\rm g}$ increase suggests that the slowdown in translational chain dynamics is directly correlated to the decreased polymer segmental motion under nanoconfinement. These findings emphasize the importance of understanding the effect of extreme nanoconfinement on the transport and thermal properties of polymers, even in weakly interacting systems, which in turn will provide guidelines in optimizing processing parameters and properties of the resulting CaRI nanocomposite

INTRODUCTION

Physical confinement of polymers occurs in a wide range of applications including nanostructured polymers in solar cells, 1,2 electronic components,³ protective coatings,^{4,5} energy storage devices, and separation systems. Confinement of polymers to nanoscopic dimensions⁸ can induce drastic changes in their properties and dynamics. In some cases, confinement-induced changes can be deleterious for the final applications of confined polymers due to their poor structural integrity relative to the bulk. For instance, polymers intercalated in between graphene oxide sheets have lower decomposition temperature than their bulk counterparts. 10 Polymer chains confined in thin films show reduced elastic modulus and fracture strength with decreasing thickness. 11-13 Thus, to enable new applications and to circumvent potential pitfalls that may result from unexpected changes in the properties of confined polymers, it is extremely important to understand the effect of physical confinement on the properties of polymers.

Nanocomposites made of mixtures of polymers and nanoparticles represent one common system in which nanoparticles can impose physical constraint on the polymer chains. In particular, when there is a high volume fraction of nanoparticles and the nanoparticles are small, a large volume fraction of polymers present in the composite lies in the confined region between nanoparticles.9 When the volume fraction of the nanoparticles is above a certain limit (for example, 50 vol %), the interparticle distance can become comparable to or smaller than the characteristic size of the

polymer chains, 14-18 inducing significant confinement on the polymer chains, which results in changes in the dynamics and mechanical properties of polymers.9 Interestingly, several naturally occurring nanocomposites have emergent properties that stem from the presence of extremely large volume fractions of nanoparticles and small fractions of highly confined polymer phase. Nacre, for example, known for its ultrahigh strength and toughness, is made of more than 90 vol % rigid nanoplatelets and less than 10% of proteinaceous polymers.

Capillary rise infiltration (CaRI) relies on the infiltration of polymers into dense nanoparticle packings via capillarity and thus enables manufacturing of nanocomposite films with extremely high volume fractions of nanoparticles (>50 vol %) with a relatively simple procedure. 5,19-23 The CaRI method circumvents processing challenges associated with the fabrication of highly filled nanocomposites using conventional methods such as compounding and layer-by-layer assembly.^{24,25} Moreover, CaRI represents a powerful method to induce extreme nanoconfinement of polymers because the characteristic pore size in the disordered packings of spherical nanoparticles is approximately 30% of the nanoparticle size, 26 which can be comparable to or smaller than the dimension of unperturbed polymer chains. In other words, CaRI enables a simple approach of confining polymers in extremely small

Received: May 7, 2018 Revised: June 20, 2018 Published: July 3, 2018



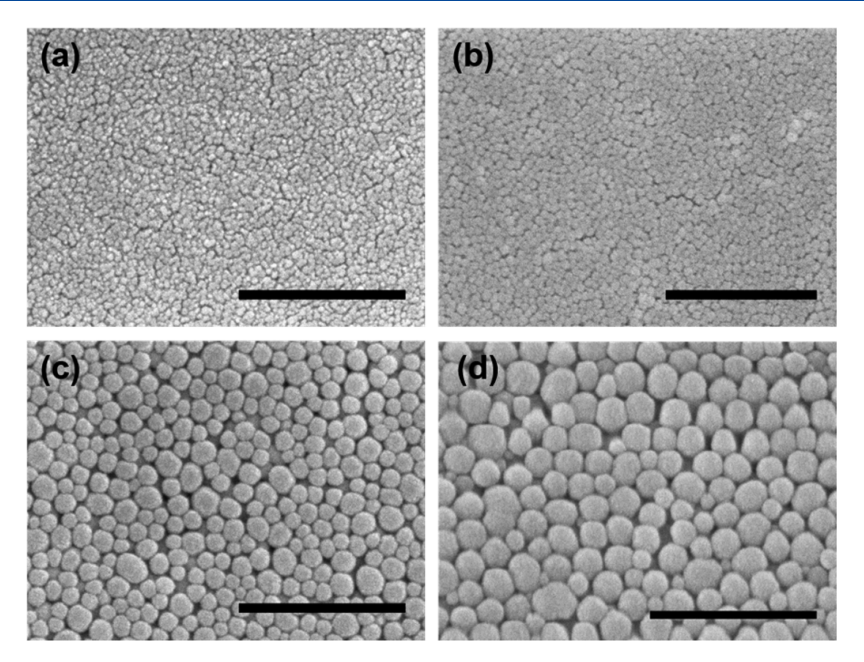


Figure 1. SEM images of SiO₂ nanoparticle films with various diameters: (a) 9 nm (measured 8.6 ± 1.3 nm), 33 (b) 27 nm (measured 27.1 ± 4.3 nm), (c) 56 nm (measured 56.1 ± 11.5 nm), and (d) 77 nm (measured 77.4 ± 14.0 nm). All scale bars are 500 nm. See the Supporting Information for measurement of NP size distribution for NPs in (b-d).

Table 1. Silica Nanoparticle Label, Measured Average Diameter (See Supporting Information), Average Pore Radius When Densely Packed, and the Confinement Ratio, $CR = R_g/R_{pore}$ for 8K PS $(R_g \sim 2.5 \text{ nm})$ and 21K PS $(R_g \sim 4 \text{ nm})^a$

silica nanoparticle label	measured diameter (nm)	average pore radius, R_{pore} (nm)	$CR_{8K PS}$	CR_{21KPS}
9 nm	8.6 ± 1.3	1.3 ± 0.2	1.88 ± 0.27	3.05 ± 0.44
27 nm	27.1 ± 4.3	3.9 ± 0.6	0.63 ± 0.10	1.02 ± 0.16
56 nm	56.1 ± 11.5	8.1 ± 1.7	0.30 ± 0.06	0.49 ± 0.10
77 nm	77.4 ± 14.0	11.2 ± 2.0	0.22 ± 0.04	0.35 ± 0.06

^aThe average diameters of the nanoparticles are determined from SEM images (see Supporting Information) and from the literature.³³

pores (<10 nm), comparable to the polymer's radius of gyration ($R_{\rm g}$), and tuning of average pore radius ($R_{\rm pore}$) based on nanoparticle sizes; i.e., smaller nanoparticles confine the polymer more strongly. To enable efficient production of CaRI nanocomposites, it is critical to understand the effect of extreme nanoconfinement on the capillarity-based transport phenomena.

In this work, we study the effect of physical nanoconfinement on the unentangled polymer viscosity during capillary rise infiltration (CaRI). We focus on unentangled polymers to rule out the effect of polymer disentanglement, which has been attributed to enhanced mobility of confined polymers in prior studies.²⁷⁻²⁹ Unentangled polymer networks with reversible bonds have been shown to exhibit self-healing properties³⁰ and hence could potentially be useful for the generation of bioinspired nanocomposites. For our experimental systems, we use polystyrene (PS) and silica nanoparticles (SiO₂ NPs), which have weak polymer-nanoparticle interaction. In our prior work, we showed that physical confinement effects dominate over polymer-nanoparticle interactions in affecting the polymer infiltration dynamics.²³ We have also shown that confinement effects dominate over free surface effects in determining the glass transition temperature of weakly interacting polymers in undersaturated CaRI composite films.³¹ Thus, this weakly interacting PS-SiO₂ NP pair represents an ideal model system to study the effect of physical confinement on the CaRI dynamics and glass

transition temperature of polymers by systematically varying the relative sizes of pores and polymers. We tune the confinement ratio (CR), defined as the ratio of the bulk polymer $R_{\rm g}$ to the $R_{\rm pore}$, by using combinations of unentangled PS with various molecular weights and ${\rm SiO_2}$ NPs of varying diameters. We show that under extreme nanoconfinement unentangled PS exhibits higher-than-bulk viscosity and glass transition temperature ($T_{\rm g}$). Specifically, we observe increasing confined polymer viscosity and $T_{\rm g}$ with CR until CR \sim 1, i.e., when $R_{\rm g}$ is comparable to $R_{\rm pore}$, above which the confined polymer viscosity and $T_{\rm g}$ values plateau. The similar trends observed in the viscosity and $T_{\rm g}$ of unentangled PS suggest that the slowdown in the chain dynamics is strongly correlated to the slowdown in the segmental dynamics.

RESULTS

Polymer Capillary Rise Infiltration (CaRI) Dynamics.

We generate bilayer films composed of a disordered dense packing of silica NPs atop a polystyrene (PS) film. We use unentangled polystyrene with molecular weights ~8000 g mol $^{-1}$ (8K) and ~21 000 g mol $^{-1}$ (21K), with radii of gyration ($R_{\rm g}$) of ~2.5 and ~4.0 nm, respectively, calculated based on the Kuhn segment length of each polymer. We use SiO $_{\rm 2}$ NPs with various diameters as shown in Figure 1 to generate different average pore radii ($R_{\rm pore}$) in which the polymer is confined. The $R_{\rm pore}$ is estimated based on $R_{\rm pore}$ = 0.29 $R_{\rm NP}$, where $R_{\rm NP}$ refers to the NP radius. The confinement ratio

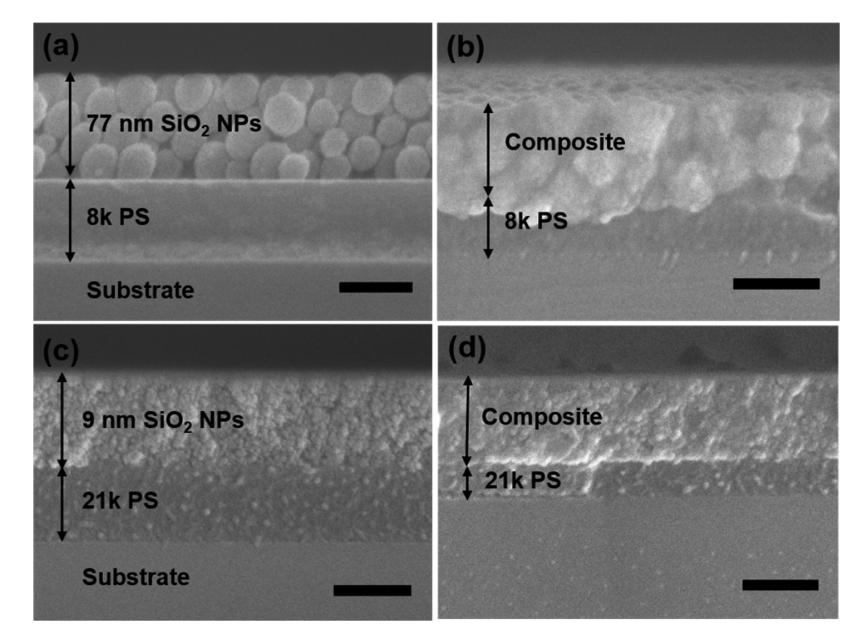


Figure 2. Cross-sectional SEM images of bilayer films of (a, b) 77 nm SiO₂ NPs atop 8K PS, (a) before and (b) after CaRI, respectively; (c, d) 9 nm SiO₂ NPs atop 21K PS (c) before and (d) after CaRI, respectively. These two systems represent the lowest and highest confinement ratios (CR = 0.22 and CR = 3.05, respectively) tested in this work. All scale bars are 200 nm.

(CR) of polymer in the disordered SiO₂ NP packing is estimated as CR = $R_{\rm g}/R_{\rm pore}$, as listed in Table 1. With the polymers and NPs used in this work, the value of CR ranges from 0.2 to 3.1. Since PS interacts weakly with SiO₂ NP, we can rule out the possible role of polymer—NP interactions and focus on the effect of physical confinement. Moreover, under extreme nanoconfinement of CaRI, the effect of physical confinement has been shown to affect the overall polymer chain and segmental dynamics more significantly than polymer—NP interactions.²³ The bilayer film consisting of the SiO₂ NP packing on top of a PS film is annealed above the polymer glass transition temperature ($T_{\rm g}$) to induce polymer wicking into the interstitial spaces in the disordered NP packing.

Figure 2 shows the cross-sectional SEM images of bilayer films representing the extreme cases where the polymer is the least confined (77 nm SiO_2 NP/8K PS, CR = 0.22) and where the polymer is the most confined (9 nm SiO_2 NP/21K PS, CR = 3.05), before and after CaRI. We observe that the polymer layer becomes thinner after the polymer infiltrates the voids in the disordered NP packing. The outline of the SiO_2 NP also appears less defined as the polymer now covers the NPs, which confirms the polymer infiltration process. The packing density of the NP packing is not altered by the CaRI process, as the average distance between the NPs remains constant following polymer infiltration. 23

We study the dynamics of polymer CaRI using *in situ* spectroscopic ellipsometry, as previously described. 19,21,23 During the annealing process, we monitor and collect the ellipsometry data on the bilayer sample. By analyzing the amplitude ratio (ψ) and phase difference (Δ) based on a three-layer Cauchy model, we track the changes in the thickness of the SiO₂ NP composite (i.e., PS-infiltrated SiO₂ NP packing) and the PS layers. To reduce the degrees of freedom and ensure solution uniqueness in the model, we determine and fix the refractive indices of the SiO₂ NP and PS layers from measurements at ~383 K to account for polymer layer thermal

expansion and the evaporation of condensed water in the interstices of the SiO_2 NP packing.

Figure 3a shows the thickness changes of the SiO_2 NP layer, composite layer, and the polymer layer with annealing time in the 77 nm SiO_2 NP/8K PS system. During CaRI, polymer infiltrates into the voids of the NP packing, causing the

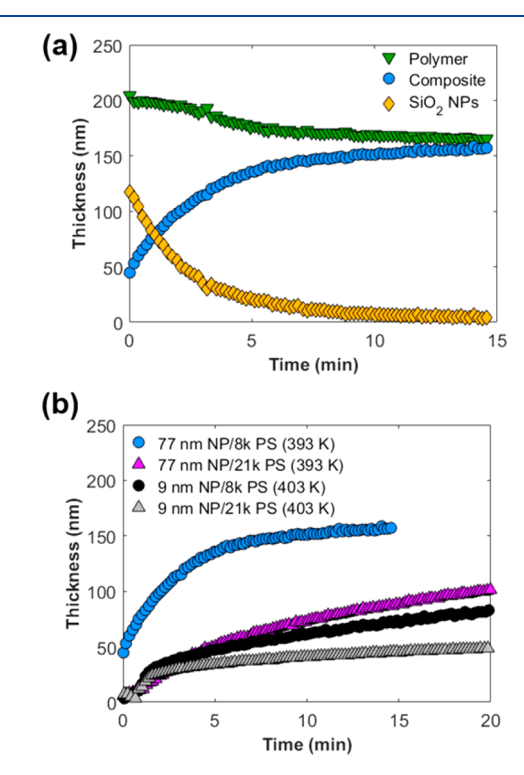


Figure 3. Thickness profile of the SiO_2 NPs, composite, and polymer layers during CaRI in 8K PS/77 nm NP at 393 K. (b) Composite layer thickness profile during CaRI in 8K PS/77 nm NPs (393 K), 21K PS/77 nm NPs (393 K), 8K PS/9 nm NPs (403 K), and 21K PS/9 nm NPs (403 K).

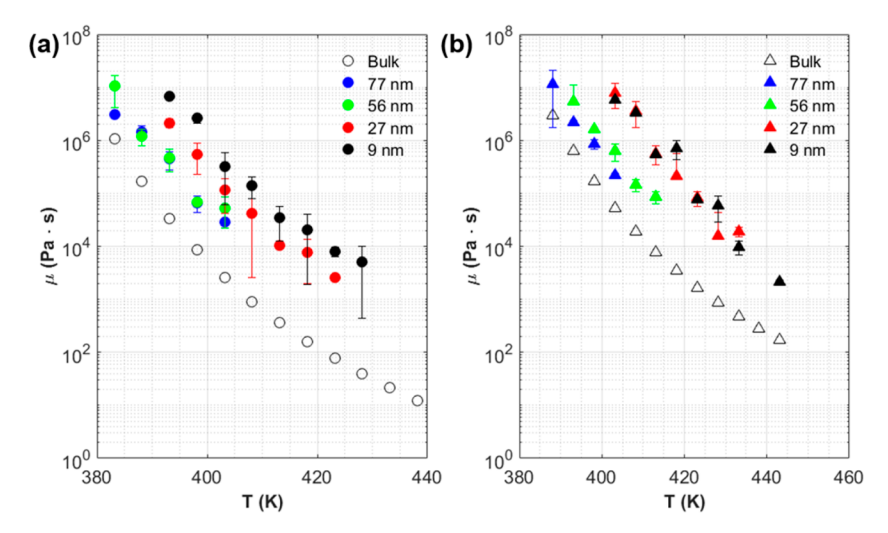


Figure 4. Bulk and confined polymer viscosity for (a) 8K PS and (b) 21K PS as a function of temperature. The confined polymer data (filled markers) is labeled by the measured NP diameter constituting the NP packing. Each data point for the confined polymer viscosities are an average of at least two runs, and the error bar represents one standard deviation. The bulk viscosity values are obtained from the literature (see Supporting Information).⁴³

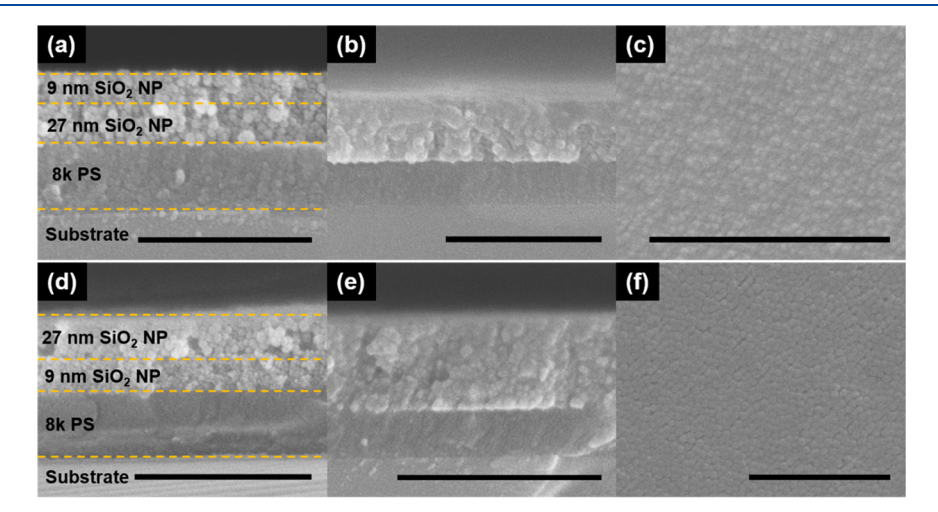


Figure 5. Top row: cross-sectional SEM images of the 9 nm/27 nm SiO_2 NP on 8K PS (a) before and (b) after CaRI; (c) top view after CaRI. Bottom row: cross-sectional SEM images of 27 nm/9 nm SiO_2 NP on 8K PS (d) before and (e) after CaRI; (f) top view after CaRI. Dotted line in (a) and (d) outlines the interfaces between distinct SiO_2 NP layers, polymer layer, and the substrate. All scale bars are 500 nm.

thickness of the bottommost polymer layer to decrease, consistent with the SEM images in Figure 2. The ellipsometry model distinguishes between the unfilled and filled SiO₂ packings (i.e., the composite layer) based on the respective refractive indices and shows that upon thermal annealing the composite layer thickness increases as polymer invades the SiO₂ NP packing with a sharp front. Figure 3b shows representative composite layer thickness change for combinations of 77 nm SiO₂ NP, 9 nm SiO₂ NP, 8K PS, and 21K PS, where we observe varying rates of infiltration of polymers. Past work has shown that the polymer CaRI can be modeled using the Lucas—Washburn model, which describes the capillarity-driven infiltration dynamics of liquids into porous media: ^{19–21,34–39}

$$h^2 = \frac{\sigma R_{\text{pore}} \cos \theta}{4\tau^2 u} t$$

The parameters in the prefactor are physical parameters describing the interaction between the polymer and the NP

surface (σ is the polymer surface tension and θ is the contact angle of the polymer on the NP surface), the pore geometry $(R_{\text{pore}} \text{ is the average pore radius and } \tau \text{ is the tortuosity of the}$ infiltration path), and the polymer property (μ is the viscosity). Thus, plotting the thickness of the composite squared (h^2) as a function of time (t) and using the physical parameters from the literature $^{26,27,40-42}$ enable us to infer the apparent viscosity of PS undergoing CaRI. 19,37 Table S1 in the Supporting Information summarizes the parameters we use to infer the confined polymer viscosity μ based on the Lucas-Washburn model. The average pore radius $R_{\rm pore}$ and tortuosity τ are intrinsic to the SiO2 NP packing and are estimated based on the NP radius and the packing porosity, respectively. 26,40 The porosity for the packings of SiO₂ NPs used in this study does not depend strongly on the nanoparticle size and is approximately 0.35.31 By measuring the initial and the final thickness of the polymer layer upon infiltration, we can infer directly the amount of polymer in the interstices of the NP packing, thereby inferring the porosity before infiltration. Although this approach may slightly overestimate the porosity

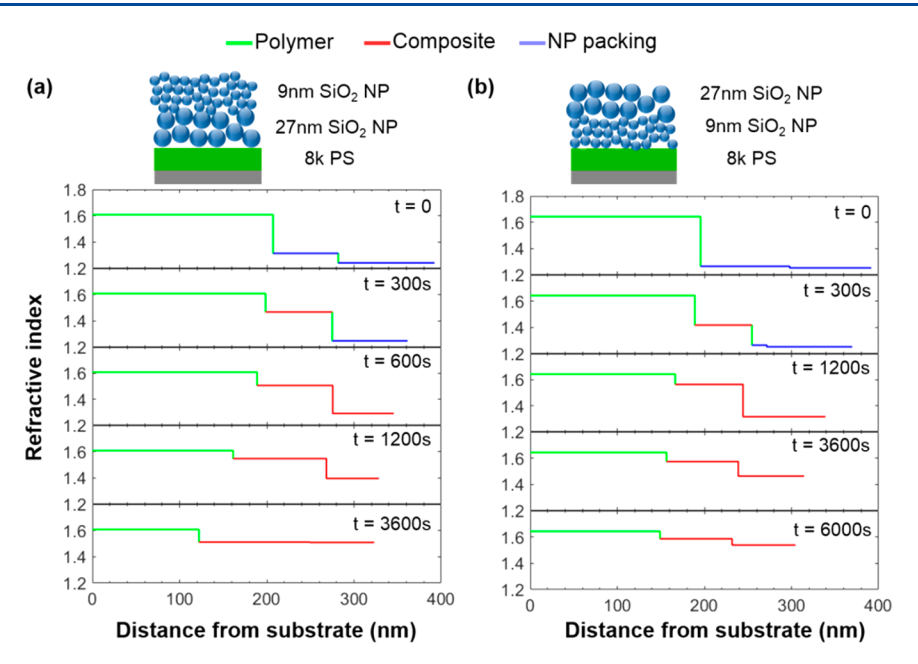


Figure 6. Plots of refractive index versus distance from the substrate for (a) 9 nm/27 nm SiO₂ NP/8K PS and (b) 27 nm/9 nm SiO₂ NP/8K PS at various stages of annealing at T = 403 K.

due to cracks in the NP films, we find that the estimated porosity is similar to that measured based on solution ellipsometry. The $R_{\rm pore}$ is estimated as 30% that of the NP radius, based on a modeling study of random packings of spheres and agglomerates of spheres. Although there are some differences in the size distribution of SiO₂ NPs used in this study, the standard deviation of pore size is less than 2 nm, and thus the four NPs used in this study provide four distinct pore sizes. The surface tension of PS is estimated based on the molecular weight and temperature of the melt. The contact angle of PS is estimated as 20° . The surface as 20° .

Effect of Physical Confinement on the Polymer Dynamics. To assess the role of physical confinement, we compare the confined and bulk polymer viscosity as a function of temperature, as shown in Figure 4. For both 8K and 21K PS, we note a significant increase of the confined polymer viscosity relative to the bulk values which are obtained from the literature.43 As the size of the NP decreases, the increase in the viscosity becomes greater, indicating that increasing the degree of physical confinement by way of decreasing the pore size (decreasing the NP size) increases the polymer viscosity. This trend is true for all cases except at the highest degree of confinement in our system, whereby we see the viscosity values approximately overlap for 9 nm SiO₂ NP/21K PS and 27 nm SiO₂ NP/21K PS. This observation suggests that there may exist a CR threshold above which the polymer viscosity plateaus. We will revisit this point later in our discussion.

To further demonstrate the role of confinement in slowing down polymer infiltration, we perform CaRI on a trilayer film, consisting of two distinct SiO_2 NP layers with different NP diameters atop a polymer layer, as shown in Figure 5. We denote 27 nm/9 nm or 9 nm/27 nm to indicate the top/bottom layer sequence of the SiO_2 NP double layers. These types of heterostructured NP packings (i.e., NP assemblies with distinct domains with different nanoparticle size, type and shapes) are important for creating multilayered Bragg reflectors $^{44-47}$ and graded structures for enhanced damage tolerance in structural coatings. When 8K PS is induced to

infiltrate these heterostructured NP packings, the dynamics of CaRI through these films is distinguishable as seen in the amplitude ratio (ψ) and phase difference (Δ) of ellipsometry data (see Supporting Information). It takes longer for the ψ and Δ of 27 nm/9 nm SiO $_2$ NP/8K PS to stop changing under the same annealing temperature (403 K), indicating longer time needed for CaRI to complete as the layer thicknesses stop changing.

Figure 6 shows the refractive index profile of the films as a function of distance from the substrate based on a four-layer Cauchy model, with each panel showing different stages of annealing. We see that the thickness of the pure PS layer decreases more rapidly in the 9 nm/27 nm SiO2 NP/8K PS sample than in the 27 nm/9 nm SiO₂ NP/8K PS sample. Because the 9 nm SiO_2 NP packing has a smaller R_{pore} , it induces a higher degree of confinement, and thus polymer infiltration through this layer becomes the rate-limiting step. As polymer infiltrates the 27 nm/9 nm SiO₂ NP packing, the ratelimiting step occurs early in the process and subsequently limits the amount of polymer available to fill the voids in the next 27 nm SiO₂ NP layer. In contrast, in the case of 9 nm/27 nm SiO₂ NP packing, polymer infiltrates the bottom 27 nm SiO₂ NP layer relatively quickly, and the rate-limiting infiltration only affects the top half of the film, thus leading to overall faster polymer infiltration throughout the film.

Polymer viscosity inferred from the Lucas—Washburn model represents the translational dynamics of the polymer as it undergoes CaRI in disordered NP packings. Our prior study showed that changes in the viscosity of polymers undergoing CaRI were correlated to their glass transition temperature ($T_{\rm g}$), which provides information on their segmental relaxation under nanoconfinement. To test whether such a correlation is retained over a wide range of CRs that we test in this study, we determine the $T_{\rm g}$ from fully annealed films—which now consist of a composite layer atop a residual polymer layer, via spectroscopic ellipsometry (see Supporting Information), a well-established technique to accurately determine $T_{\rm g}$ of polymers in confined geometries. $^{23,31,50-53}$ We use a two-

layer Cauchy model describing the composite and polymer layers to analyze the ellipsometry data. Figure 7 shows the

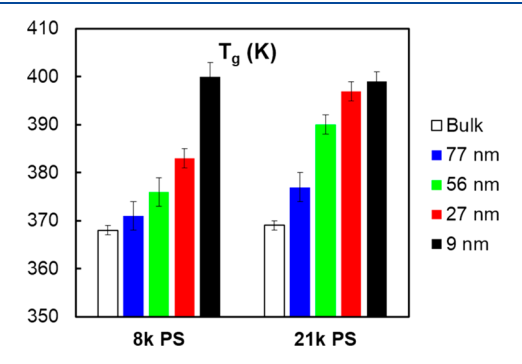


Figure 7. Glass transition temperature (T_g) of 8K and 21K PS in the bulk and in the confined state, labeled by the measured NP diameter constituting the NP packing.

confined polymer $T_{\rm g}$ as a function of NP size compared with the bulk polymer $T_{\rm g}$ determined using DSC. For both polymers, we observe increased $T_{\rm g}$ for confined polymer relative to the bulk. Moreover, the increase in $T_{\rm g}$ ($\Delta T_{\rm g}$) increases as the NP size is decreased (and hence higher CR). This trend confirms once again that the increase in polymer viscosity is highly correlated to decreased segmental mobility of polymer under nanoconfinement.

DISCUSSION

Weakly interacting polymer/NP or polymer/substrate systems such as PS/SiO₂ have been widely used in nanocomposite, nanochannels, and thin film geometries to understand polymer behavior under confinement. Many thin film studies have reported decreasing $T_{\sigma}^{50,54-56}$ and viscosity⁵⁷ with decreasing PS film thickness. These observations are attributed to the enhanced free surface (i.e., polymer/air) dynamics which dominates the overall chain dynamics of the system. 54,56,58 In nanocomposite systems, there have been numerous reports of slowdown 16,17,59 and also some reports of bulk-like (i.e., no changes due to confinement) chain diffusivity⁶⁰ and segmental motion⁶¹ near the NP surfaces. For highly entangled PS (typical MW > 10^2 kg/mol) in anodic aluminum oxide (AAO) nanochannels, another interesting geometry with weak interaction between PS and solid surface, increased chain mobility (i.e., reduced viscosity) has been previously reported, 27 which is in stark contrast to our observations. We attribute such discrepancy to the difference in the confinement geometry and disentanglement effects. Instead of transporting through straight, cylindrical channels in the AAO templates, PS undergoing CaRI in disordered NP packings transports through tortuous pathways with variable pore sizes. The narrow regions within the packing may act as entropic barriers, 16 whereby the polymers have to undergo substantial conformational changes to squeeze through. Another possibility is that as the polymer infiltrates through pores with varying cross-sectional area, the transport of polymer is affected by elongational deformation of the polymer chains; that is, the inferred viscosity could have both the extensional and the shear components.⁶² The enhanced mobility of the highly entangled polymer in the cylindrical pores of the AAO membranes has been attributed to disentanglement effects, whereby confinement decreases the entanglement density, leading to facilitated transport. 27,28,63

Since we use unentangled polymers, we do not expect this latter mechanism to play a significant role.

Although we have successfully infiltrated long chain, entangled polymers into NP packings, ^{19,31} the infiltration behavior of these highly entangled polymers appears distinct from the capillary rise behavior in this current study. Thus, we focus our current study on unentangled polymers, with 21K PS being close to the entanglement molecular weight. ⁶⁴ Our ongoing work focuses on understanding the infiltration behavior of high molecular weight, entangled polymer in nanoparticle packings.

There are also contradictory reports of increased, 23,31,65 decreased, $^{66-68}$ and mixed behaviors of multiple $T_{\rm g}$'s 69,70 in nanocomposites and nanopores. T_g of PS in AAO templates with 55-250 nm pores has been observed to increase (up to 379 K), which is attributed to the geometric curvature of the wall decreasing the interchain proximity.⁶⁵ Our previous work also showed increased $T_{\rm g}$ of PS in undersaturated CaRI (UCaRI) nanocomposites; i.e., NP packing is partially filled with the polymer. Despite the presence of the polymer-air free surface in these UCaRI nanocomposites, the increased T_{σ} is attributed to the formation of polymer capillary bridges in the neck regions of the NP contact points and thus a more amplified confinement effect.³¹ When infiltrating the NP packing, we expect the PS to be in contact with multiple NPs; this similar bridging effect may explain the increase in viscosity and T_g we see in our CaRI films and the undersaturated films.31

While Figures 4 and 7 show qualitatively similar trends across 8K and 21K PS upon confinement, such that both polymers exhibit increased viscosity and $T_{\rm g}$ when infiltrating NP packings with decreasing NP size, we can further generalize the role of physical confinement by assessing the normalized polymer viscosity and the change in $T_{\rm g}$ as a function of confinement ratio (CR), as shown in Figure 8. Similar confinement parameters have been used previously to scale the effect of physical confinement on the translational mobility of polymers in nanocomposites. $^{14,16-18}$ To test the validity of the trends, we perform additional CaRI and $T_{\rm g}$ measurements using 13K and 19K PS.

We observe that both normalized viscosity $(\mu_{\text{confined}}/\mu_{\text{bulk}})$ (Figure 8a) and change in $T_{\rm g}$ ($\Delta T_{\rm g}$) (Figure 8b) show increasing trends, more or less linearly, before saturating at CR \sim 1, i.e., when the $R_{\rm g}$ is comparable to $R_{\rm pore}$. From the initial slope of Figure 6b, we estimate and predict the recovery of the bulk viscosity and $T_{\rm g}$ at low CR (CR ~ 0.1), which suggests that the selection of a NP \sim 30 times the size of R_{σ} would eliminate the physical confinement effect (i.e., recovery of bulk viscosity and T_g). This CR would correspond to 150 and 240 nm diameter NPs for 8K and 21K PS, respectively. This prediction agrees qualitatively with the previously reported universal scaling of polymer diffusion in polymer nanocomposites, where polymer diffusion is slowed down when the interparticle spacing is approximately 20 times or smaller than the polymer R_g^{14} Another study of PS thin film near oxide-covered silicon reports decreased diffusion which persist up to $10R_g$ from the interface.⁷¹

To test the recovery of bulk-like viscosity, we perform CaRI on 196 nm SiO₂ NPs/21K PS (CR \sim 0.14) and 130 nm SiO₂ NPs/8K PS (CR \sim 0.13) bilayer films and compare the infiltration heights of PS obtained experimentally with the calculated height, assuming bulk polymer viscosity at the annealing temperature. As shown in the Supporting

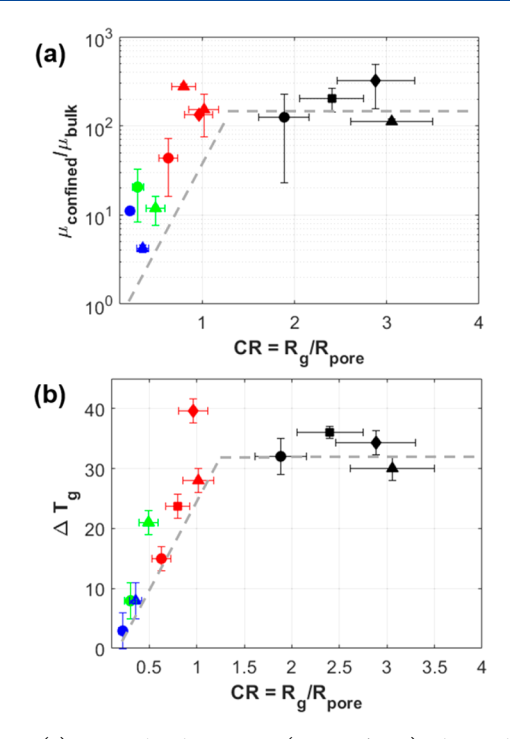


Figure 8. (a) Normalized viscosity $(\mu_{\text{confined}}/\mu_{\text{bulk}})$ obtained for PS undergoing CaRI at T=403 K and the (b) ΔT_{g} $(T_{\text{g}}-T_{\text{g,bulk}})$ as a function of confinement ratio (CR). The lines are to guide the eye.

Information, we find qualitatively good agreement between our predictions and the experiments; annealing the 196 nm SiO₂ NP/21K PS and 130 nm SiO₂ NP/8K PS bilayer films at 383 K for 3.5 h and 18 min, respectively, led to infiltration height of ~210 nm, similar to the infiltration height of 200 nm which is predicted by the Lucas-Washburn analysis assuming bulk polymer viscosity. Below CR of 1 (CR < 1), the increasing trend in the normalized polymer viscosity with CR suggests that physical confinement strongly and systematically affects the translational motion of the chains. This slowdown may be associated with the entropic barrier, whereby the segments of the infiltrating chains lose entropy when stretching to squeeze through the narrow neck regions in the NP packing. 16 In the 9 nm SiO₂ NP packing, we see 8K and 21K PS having comparable viscosity, suggesting that the physical confinement imposed by the NPs plays a more significant role than the polymer size or molecular weight. Furthermore, from Figure 4b, we see that in 21K PS the viscosity is comparable in 9 and 27 nm SiO₂ NP packings, consistent with the trends in Figure 8. These observations suggest that when the size of the polymer is similar to or larger than the pore size, the bottleneck process is the same and may be related to the slowest segmental motion. To further understand this intriguing observation, our ongoing work focuses on developing a theoretical framework of CaRI to account for the conformational entropy loss of chain due to confinement and gain in free energy due to wetting of polymer on the pore surface.

CONCLUSION

In this work, we study the role of physical confinement on the polymer viscosity and the glass transition temperature in composites prepared via capillary rise infiltration (CaRI) of unentangled polymers in random packing of weakly interacting nanoparticles. The confinement ratio (CR), defined as the ratio of the polymer radius of gyration (R_{σ}) to the average pore

radius in the disordered nanoparticle packing (R_{pore}) , is tuned by using four polystyrenes with distinct molecular weights and SiO₂ NPs of four different diameters. We observe increased viscosity and T_g of polymer relative to the bulk under nanoconfinement. Deviations of viscosity and T_g relative to the bulk values increase with CR until an upper threshold of CR ~ 1 is reached. Overall, the correlation between the viscosity and T_{g} increase suggests the slowdown of translational motion of polymers is strongly influenced by the slowdown of the segmental motion. Furthermore, we show that the physical confinement effect saturates when the polymer R_{σ} is equal to or greater than the R_{pore} , such that the viscosity and T_{g} no longer increase. Our work provides a fundamental framework to optimize processing parameters such as temperature and annealing time for scalable manufacturing of polymerinfiltrated nanoparticle films using CaRI. Our results also provide important guidelines in tailoring the processing conditions when heterostructured or hierarchically structured porous materials are infiltrated with polymers.

■ MATERIALS AND METHODS

Materials. Polystyrene (PS) (8K PS, $M_n = 8000 \text{ g mol}^{-1}$, PDI = 1.10; 21K PS, $M_n = 21\,000 \text{ g mol}^{-1}$, PDI = 1.04) is purchased from Polymer Source Inc. 13K PS $(M_w = 13\,000 \text{ g mol}^{-1}, \text{PDI} = 1.06)$ is purchased from Pressure Chemical Company, whereas 19K PS ($M_{\rm w}$ = 18 700 g mol⁻¹) is purchased from Aldrich Chemical Co. Aqueous suspensions of silica nanoparticles (SiO2 NPs) with diameters of 9 nm (LUDOX SM-30, 30 wt % suspension in water) and 27 nm (LUDOX TM-50, 50 wt % suspension in water) are purchased from Sigma-Aldrich, whereas those with diameters 56 nm (SNOWTEX ST-OL silica, 29.6 wt % suspension in water) and 77 nm (SNOWTEX ST-YL silica, 40.4 wt % suspension in water) are obtained from Nissan Chemical America Corp. The 130 and 196 nm SiO₂ NPs are synthesized using a modified Stöber method. 72,73 The NP size distribution is determined from the literature³³ and using scanning electron microscopy (SEM) image analysis (see Supporting Information).

Preparation and Characterization of Nanoparticle/Polymer Bilayer and Trilayer Films. Silicon wafers are cut into approximately 1 cm \times 1 cm squares. The wafers are rinsed with acetone, isopropanol, and deionized water and dried with air, before further cleaned by oxygen plasma treatment for \sim 5 min. 6 wt % PS solution is prepared by dissolving PS in toluene. The SiO₂ NP suspension is diluted to 10–15 wt % using water. All solutions are bath-sonicated for at least 2 h and filtered prior to use. The 200 nm thick PS layer is deposited by spin-coating the 6 wt % PS solution at 3000 rpm for 30 s onto the cleaned silicon wafer using a WS-400BZ-6NPP/Lite spin-coater from Laurell Technologies Corporation. Then, the polymer film is oxygen plasma-treated for \sim 2 s to render the film surface hydrophilic, on which the SiO₂ NP suspension is deposited is spin-coated at 3000 rpm for 30 s to generate an \sim 200 nm thick SiO₂ NP layer.

To generate trilayer samples consisting of two sequentially deposited SiO $_2$ NP packings with different sizes atop \sim 200 nm thick 8K PS layer, 5 wt % suspensions of 9 and 27 nm SiO $_2$ NPs are prepared. \sim 100 nm layer of each SiO $_2$ packing is generated by spin-coating the SiO $_2$ NP suspension at 3000 rpm on the polymer film and allowed to dry at room temperature in ambient conditions for at least an hour prior to depositing the next layer.

Scanning electron microscopy (SEM) images of the samples before and after CaRI are taken using a JEOL 7500F HRSEM. The sample is sputtered with a thin gold/palladium layer using a Cressington Sputter Coater 107 prior to imaging to prevent charging. Cross-section images are taken by cleaving across the sample using a diamond scribe and mounting the sample vertically on a stub with the cross sections facing up toward the beam. The samples are imaged at

an accelerating voltage of 5 kV, emission current 20 μ A, at a working distance of ~8 mm.

Characterization of Polymer Capillary Rise Infiltration (CaRI) Process. The polymer infiltration into the voids of the NP packing is monitored in situ using a J.A. Woollam Alpha-SE spectroscopic ellipsometer, while the bilayer sample is annealed above the glass transition temperature (T_g) of the polymer using a Linkam THMS350 V heating stage, under ambient conditions. The heating stage is 22 mm in diameter, open to ambient air, and has a temperature resolution of ~1 K. The Linksys software displays the temperature and allows user to set the desired set point temperature, heating rate, and hold time for the set point temperature. To ensure good thermal contact, the sample is adhered to the heating stage using a thermal paste (Arctic Silver Ceramic polysynthetic thermal compound).⁷⁴ The ellipsometry data are collected in the wavelength (λ) range of 380–900 nm at an incident angle of 70°. The CompleteEASE software package provided by J.A. Woollam enables the analysis of the raw psi (ψ) and delta (Δ) data by fitting to a threelayer Cauchy model (nanoparticle packing, composite, polymer) on a silicon substrate with native oxide layer.^{21,44} The Cauchy model for each layer is expressed as $n(\lambda) = A + B/\lambda^2 + C/\lambda^4$ and $k(\lambda) = 0$, whereby A, B, and C are the optical constants, λ is the wavelength $[\mu m]$, and n and k are the real and imaginary components of the index of refraction, respectively. The model fitting enables translation of raw data into physical parameters describing the thickness and refractive index of each layer in the sample.⁷⁵ The temperature at which the sample is annealed is chosen to be above the $T_{\rm g}$ of the polymer, in the range of T = 383-433 K, such that the infiltration rate is still resolvable within the time resolution of the ellipsometry data.

Glass Transition Temperature Measurements. The glass transition temperature (T_g) of the polymer confined in the NP packing is measured using a J.A. Woollam M-2000V spectroscopic ellipsometer. A polymer-infiltrated film is mounted onto a Linkam THMS 600 temperature-controlled stage attached to the ellipsometer. The in situ ellipsometry sampling rate is 1 s with high accuracy zoneaveraging. Three heating and cooling cycles between 303 and 423 K under dry nitrogen flow are performed for each sample, with heating rate of 30 K/min and cooling rate of 10 K/min, respectively. $T_{\rm g}$ data are obtained from the cooling cycle. The thickness and refractive index of the sample are determined by fitting the cooling ramp raw data to the Cauchy model. The T_g of the confined polymer for each film is determined via the intersection of the linear fits to the supercooled and glassy regimes in the plots of nanocomposite refractive index versus temperature. The error is determined as the 95% confidence range of the distance between the intersection of fitting lines (see Supporting Information). Since the NP packing is minimally perturbed by the polymer infiltration process, the thickness of the composite layer is held constant during the dynamic data fit. The bulk polymer $T_{\rm g}$ is determined using the same protocol on the residual polymer layer's refractive index versus temperature. The T_g 's of the bulk polymer samples are also determined using the TA Instruments Q2000 differential scanning calorimeter (DSC). For each PS, 6 mg of PS sample is placed in a nonhermetically sealed pan, and the sample is initially cooled to 293 K, before subjecting it to two heating and cooling cycles from T = 293 K to T = 423 at 10 K/min. The T_g is defined as the midpoint of the step transition of the heat capacity and expressed as the average from the two cooling cycle measurements. The T_g values measured are in good agreement with those reported previously. 6

■ ASSOCIATED CONTENT

S Supporting Information

The Supporting Information is available free of charge on the ACS Publications website at DOI: 10.1021/acs.macromol.8b00966.

Nanoparticle size distribution, determination of bulk polystyrene viscosity from the literature, determination of confined polymer glass transition temperature (T_g)

using spectroscopic ellipsometry, raw ellipsometry data during the annealing of 9 nm/27 nm and 27 nm/9 nm SiO_2 NP/8K PS films, physical parameters for Lucas—Washburn analysis of confined polymer viscosity calculation (PDF)

AUTHOR INFORMATION

Corresponding Authors

*(Z.F.) E-mail fakhraai@sas.upenn.edu. *(D.L.) E-mail daeyeon@seas.upenn.edu.

ORCID

Jyo Lyn Hor: 0000-0002-0340-8330 Haonan Wang: 0000-0003-2047-5380 Zahra Fakhraai: 0000-0002-0597-9882 Daeyeon Lee: 0000-0001-6679-290X

Author Contributions

J.L.H., H.W., Z.F., and D.L. conceived the experiments; J.L.H. and H.W. conducted the experiments. J.L.H., H.W., Z.F., and D.L. analyzed the experimental results; Z.F. and D.L. supervised the work. The manuscript was written through contributions of all authors. All authors have given approval to the final version of the manuscript.

Notes

The authors declare no competing financial interest.

ACKNOWLEDGMENTS

This work was supported primarily by Penn MRSEC NSF-1720530 and partially by NSF-1449337, NSF-1662695, and NSF-CAREER DMR-1350044. We thank Dr. Tianyi Liu for her assistance with the differential scanning calorimetry (DSC), Prof. Karen Winey (University of Pennsylvania) for supplying 13K and 19K PS, and Katie Rose and Zhiwei Liao for synthesizing 130 and 196 nm SiO₂ nanoparticles. We also thank Nissan Chemical America Corp. for supplying the Snowtex ST-YL SiO₂ NP suspension.

ABBREVIATIONS

CaRI, capillary rise infiltration; $T_{\rm g}$, glass transition temperature; NP, nanoparticle; PS, polystyrene; $R_{\rm g}$, radius of gyration; $R_{\rm pore}$, average pore radius; CR, confinement ratio.

REFERENCES

- (1) Nejati, S.; Lau, K. K. S. Pore Filling of Nanostructured Electrodes in Dye Sensitized Solar Cells by Initiated Chemical Vapor Deposition. *Nano Lett.* **2011**, *11* (2), 419–423.
- (2) Zohrevand, A.; Ajji, A.; Mighri, F. Microstructure and Properties of Porous Nanocomposite Films: Effects of Composition and Process Parameters. *Polym. Int.* **2014**, *63* (12), 2052–2060.
- (3) Vogt, B. D. Mechanical and Viscoelastic Properties of Confined Amorphous Polymers. *J. Polym. Sci., Part B: Polym. Phys.* **2018**, *S6* (1), 9–30.
- (4) Olad, A.; Rasouli, H. Enhanced Corrosion Protective Coating Based on Conducting Polyaniline/Zinc Nanocomposite. *J. Appl. Polym. Sci.* **2010**, *115*, 2221–2227.
- (5) Manohar, N.; Stebe, K. J.; Lee, D. Solvent-Driven Infiltration of Polymer (SIP) into Nanoparticle Packings. *ACS Macro Lett.* **2017**, *6*, 1104–1108.
- (6) Gangopadhyay, R.; De, A. Conducting Polymer Nanocomposites: A Brief Overview. *Chem. Mater.* **2000**, *12* (3), *608–622*. (7) Merkel, T. C.; Freeman, B. D.; Spontak, R. J.; He, Z.; Pinnau, I.; Meakin, P.; Hill, A. J. Ultrapermeable, Reverse-Selective Nanocomposite Membranes. *Science (Washington, DC, U. S.)* **2002**, *296*, 519–522.

(8) Isaacson, S. G.; Lionti, K.; Volksen, W.; Magbitang, T. P.; Matsuda, Y.; Dauskardt, R. H.; Dubois, G. Fundamental Limits of Material Toughening in Molecularly Confined Polymers. *Nat. Mater.* **2016**, *15*, 294–298.

- (9) Winey, K. I.; Vaia, R. A. Polymer Nanocomposites. MRS Bull. **2007**, 32 (4), 314–319.
- (10) Barroso-Bujans, F.; Alegría, A.; Pomposo, J. A.; Colmenero, J. Thermal Stability of Polymers Confined in Graphite Oxide. *Macromolecules* **2013**, *46* (5), 1890–1898.
- (11) Tang, S.; Steven Greene, M.; Peng, X. H.; Liu, W. K.; Guo, Z. Y. Chain Confinement Drives the Mechanical Properties of Nanoporous Polymers. *EPL* **2014**, *106* (3), 36002.
- (12) Lee, J. H.; Chung, J. Y.; Stafford, C. M. Effect of Confinement on Stiffness and Fracture of Thin Amorphous Polymer Films. *ACS Macro Lett.* **2012**, *1* (1), 122–126.
- (13) Stafford, C. M.; Harrison, C.; Beers, K. L.; Karim, A.; Amis, E. J.; Vanlandingham, M. R.; Kim, H. C.; Volksen, W.; Miller, R. D.; Simonyi, E. E. A Buckling-Based Metrology for Measuring the Elastic Moduli of Polymeric Thin Films. *Nat. Mater.* **2004**, *3* (8), 545–550.
- (14) Choi, J.; Hore, M. J. A.; Meth, J. S.; Clarke, N.; Winey, K. I.; Composto, R. J. Universal Scaling of Polymer Diffusion in Nanocomposites. *ACS Macro Lett.* **2013**, 2 (6), 485–490.
- (15) Meth, J. S.; Gam, S.; Choi, J.; Lin, C. C.; Composto, R. J.; Winey, K. I. Excluded Volume Model for the Reduction of Polymer Diffusion into Nanocomposites. *J. Phys. Chem. B* **2013**, *117* (49), 15675–15683.
- (16) Gam, S.; Meth, J. S.; Zane, S. G.; Chi, C.; Wood, B. A.; Seitz, M. E.; Winey, K. I.; Clarke, N.; Composto, R. J. Macromolecular Diffusion in a Crowded Polymer Nanocomposite. *Macromolecules* **2011**, *44* (9), 3494–3501.
- (17) Lin, C. C.; Gam, S.; Meth, J. S.; Clarke, N.; Winey, K. I.; Composto, R. J. Do Attractive Polymer-Nanoparticle Interactions Retard Polymer Diffusion in Nanocomposites? *Macromolecules* **2013**, 46 (11), 4502–4509.
- (18) Wu, S. Phase Structure and Adhesion in Polymer Blends: A Criterion for Rubber Toughening. *Polymer* **1985**, 26 (12), 1855–1863
- (19) Huang, Y.-R.; Jiang, Y.; Hor, J. L.; Gupta, R.; Zhang, L.; Stebe, K. J.; Feng, G.; Turner, K. T.; Lee, D. Polymer Nanocomposite Films with Extremely High Nanoparticle Loadings via Capillary Rise Infiltration (CaRI). *Nanoscale* **2015**, *7* (2), 798–805.
- (20) Shavit, A.; Riggleman, R. A. The Dynamics of Unentangled Polymers during Capillary Rise Infiltration into a Nanoparticle Packing. *Soft Matter* **2015**, *11* (42), 8285–8295.
- (21) Hor, J. L.; Jiang, Y.; Ring, D. J.; Riggleman, R. A.; Turner, K. T.; Lee, D. Nanoporous Polymer-Infiltrated Nanoparticle Films with Uniform or Graded Porosity via Undersaturated Capillary Rise Infiltration. ACS Nano 2017, 11 (3), 3229–3236.
- (22) Qiang, Y.; Manohar, N.; Stebe, K. J.; Lee, D. Polymer Blend-Filled Nanoparticle Films via Monomer-Driven Infiltration of Polymer and Photopolymerization. *Mol. Syst. Des. Eng.* **2018**, *3*, 96.
- (23) Hor, J. L.; Wang, H.; Fakhraai, Z.; Lee, D. Effects of Polymer–nanoparticle Interactions on the Viscosity of Unentangled Polymers under Extreme Nanoconfinement during Capillary Rise Infiltration. *Soft Matter* **2018**, *14*, 2438–2446.
- (24) Podsiadlo, P.; Tang, Z.; Shim, B. S.; Kotov, N. A. Counterintuitive Effect of Molecular Strength and Role of Molecular Rigidity on Mechanical Properties of Layer-by-Layer Assembled Nanocomposites. *Nano Lett.* **2007**, *7* (5), 1224–1231.
- (25) Finnemore, A.; Cunha, P.; Shean, T.; Vignolini, S.; Guldin, S.; Oyen, M.; Steiner, U. Biomimetic Layer-by-Layer Assembly of Artificial Nacre. *Nat. Commun.* **2012**, *3*, 1–6.
- (26) Bertei, A.; Nucci, B.; Nicolella, C. Effective Transport Properties in Random Packings of Spheres and Agglomerates. *Chem. Eng. Trans.* **2013**, 32, 1531–1536.
- (27) Shin, K.; Obukhov, S.; Chen, J.-T.; Huh, J.; Hwang, Y.; Mok, S.; Dobriyal, P.; Thiyagarajan, P.; Russell, T. P. Enhanced Mobility of Confined Polymers. *Nat. Mater.* **2007**, *6* (12), 961–965.

(28) Sussman, D. M.; Tung, W.; Winey, K. I.; Schweizer, K. S.; Riggleman, R. A. Entanglement Reduction and Anisotropic Chain and Primitive Path Conformations in Polymer Melts under Thin Film and Cylindrical Confinement. *Macromolecules* **2014**, *47* (18), 6462–6472.

- (29) Tung, W.-S.; Composto, R. J.; Riggleman, R. A.; Winey, K. I. Local Polymer Dynamics and Diffusion in Cylindrical Nanoconfinement. *Macromolecules* **2015**, *48* (7), 2324–2332.
- (30) Stukalin, E. B.; Cai, L. H.; Kumar, N. A.; Leibler, L.; Rubinstein, M. Self-Healing of Unentangled Polymer Networks with Reversible Bonds. *Macromolecules* **2013**, *46* (18), 7525–7541.
- (31) Wang, H.; Hor, J. L.; Zhang, Y.; Liu, T.; Lee, D.; Fakhraai, Z. Dramatic Increase In Polymer Glass Transition Temperature Under Extreme Nanoconfinement In Weakly-Interacting Nanoparticle Films. *ACS Nano* **2018**, DOI: 10.1021/acsnano.8b01341.
- (32) Rubinstein, M.; Colby, R. H. Polymer Physics; Oxford University Press: Oxford, UK, 2003.
- (33) Lee, D.; Gemici, Z.; Rubner, M. F.; Cohen, R. E. Multilayers of Oppositely Charged SiO₂ Nanoparticles: Effect of Surface Charge on Multilayer Assembly. *Langmuir* **2007**, 23 (17), 8833–8837.
- (34) Dimitrov, D. I.; Milchev, A.; Binder, K. Capillary Rise in Nanotubes Coated with Polymer Brushes. *Ann. N. Y. Acad. Sci.* **2009**, 1161, 537–548.
- (35) Engel, M.; Stühn, B. In Situ Small Angle X-Ray Scattering Measurements of the Filling Process of Polyisobutylene and Poly-Epsilon-Caprolactone in Ion Track Etched Polycarbonate Nanopores. *J. Chem. Phys.* **2010**, *1*32 (22), 224502.
- (36) De Jongh, P. E.; Eggenhuisen, T. M. Melt Infiltration: An Emerging Technique for the Preparation of Novel Functional Nanostructured Materials. *Adv. Mater.* **2013**, 25 (46), 6672–6690.
- (37) Suh, K. Y.; Kim, P.; Eui Jeong, H.; Kwan Kim, J. Measurement of Viscosity of Confined Polymer Melt Using Capillary Kinetics. *Nanoscale Microscale Thermophys. Eng.* **2006**, *10* (3), 263–274.
- (38) Yao, Y.; Butt, H.-J.; Zhou, J.; Doi, M.; Floudas, G. Capillary Imbibition of Polymer Mixtures in Nanopores. *Macromolecules* **2018**, *51* (8), 3059–3065.
- (39) Cao, B.-Y.; Yang, M.; Hu, G.-J. Capillary Filling Dynamics of Polymer Melts in Nanopores: Experiments and Rheological Modelling. *RSC Adv.* **2016**, *6* (9), 7553–7559.
- (40) Rémond, S.; Gallias, J. L.; Mizrahi, A. Characterization of Voids in Spherical Particle Systems by Delaunay Empty Spheres. *Granular Matter* **2008**, *10* (4), 329–334.
- (41) Dee, G. T.; Sauer, B. B. The Molecular Weight and Temperature Dependence of Polymer Surface Tension: Comparison of Experiment with Interface Gradient Theory. *J. Colloid Interface Sci.* **1992**, *152* (1), 85–103.
- (42) Seemann, R.; Jacobs, K.; Blossey, R. Polystyrene Nanodroplets. *J. Phys.: Condens. Matter* **2001**, *13*, 4915–4923.
- (43) Fox, T. G.; Flory, P. J. Viscosity-Molecular Weight and Viscosity-Temperature Relationships for Polystyrene and Polyisobutylene. J. Am. Chem. Soc. 1948, 70 (7), 2384–2395.
- (44) Huang, Y.-R.; Park, J. T.; Prosser, J. H.; Kim, J. H.; Lee, D. Multifunctional All-TiO $_2$ Bragg Stacks Based on Blocking Layer-Assisted Spin Coating. *J. Mater. Chem. C* **2014**, *2*, 3260.
- (45) Prosser, J. H.; Brugarolas, T.; Lee, S.; Nolte, A. J.; Lee, D. Avoiding Cracks in Nanoparticle Films. *Nano Lett.* **2012**, *12* (10), 5287–5291.
- (46) Park, J. T.; Prosser, J. H.; Kim, D. J.; Kim, J. H.; Lee, D. Bragg Stack-Functionalized Counter Electrode for Solid-State Dye-Sensitized Solar Cells. *ChemSusChem* **2013**, *6* (5), 856–864.
- (47) Wu, Z.; Lee, D.; Rubner, M. F.; Cohen, R. E. Structural Color in Porous, Superhydrophilic, and Self-Cleaning SiO 2/TiO₂′ Bragg Stacks. *Small* **2007**, *3* (8), 1445–1454.
- (48) Vitale Brovarone, C.; Verné, E.; Krajewski, A.; Ravaglioli, A. Graded Coatings on Ceramic Substrates for Biomedical Applications. *J. Eur. Ceram. Soc.* **2001**, *21* (16), 2855–2862.
- (49) Bruet, B. J. F.; Song, J.; Boyce, M. C.; Ortiz, C. Materials Design Principles of Ancient Fish Armour. *Nat. Mater.* **2008**, 7 (9), 748–756.

(50) Forrest, J. A.; Dalnoki-Veress, K.; Stevens, J. R.; Dutcher, J. R. Effect of Free Surfaces on the Glass Transition Temperature of Thin Polymer Films. *Phys. Rev. Lett.* **1996**, 77 (10), 2002–2005.

- (51) Napolitano, S.; Glynos, E.; Tito, N. B. Glass Transition of Polymers in Bulk, Confined Geometries, and near Interfaces. *Rep. Prog. Phys.* **2017**, 80 (3), 036602.
- (\$\frac{5}{2}\$) Efremov, M. Y.; Soofi, S. S.; Kiyanova, A. V.; Munoz, C. J.; Burgardt, P.; Cerrina, F.; Nealey, P. F. Vacuum Ellipsometry as a Method for Probing Glass Transition in Thin Polymer Films. *Rev. Sci. Instrum.* **2008**, 79 (4), 043903.
- (53) Beaucage, G.; Composto, R.; Stein, R. S. Ellipsometric Study of the Glass Transition and Thermal Expansion Coefficients of Thin Polymer Films. *J. Polym. Sci., Part B: Polym. Phys.* **1993**, 31 (3), 319–326.
- (54) Glor, E. C.; Fakhraai, Z. Facilitation of Interfacial Dynamics in Entangled Polymer Films. *J. Chem. Phys.* **2014**, *141* (19), 194505.
- (55) Wang, J.; McKenna, G. B. Viscoelastic and Glass Transition Properties of Ultrathin Polystyrene Films by Dewetting from Liquid Glycerol. *Macromolecules* **2013**, 46 (6), 2485–2495.
- (56) Keddie, J. L. I.; Jones, R. A. L.; Cory, R. A. Size-Dependent Depression of the Glass Transition Temperature in Polymer Films. *Europhys. Lett.* **1994**, 27 (July), 59–64.
- (57) Chen, F.; Peng, D.; Lam, C.-H.; Tsui, O. K. C. Viscosity and Surface-Promoted Slippage of Thin Polymer Films Supported by a Solid Substrate. *Macromolecules* **2015**, *48* (14), 5034–5039.
- (58) Fakhraai, Z.; Forrest, J. A. Measuring the Surface Dynamics. Science (Washington, DC, U. S.) 2008, 319, 600-605.
- (59) Li, Y.; Kröger, M.; Liu, W. K. Dynamic Structure of Unentangled Polymer Chains in the Vicinity of Non-Attractive Nanoparticles. *Soft Matter* **2014**, *10* (11), 1723–1737.
- (60) Franz, C.; Lange, F.; Golitsyn, Y.; Hartmann-azanza, B.; Steinhart, M.; Krutyeva, M.; Saalwächter, K. Chain Dynamics and Segmental Orientation in Polymer Melts Confined to Nanochannels. *Macromolecules* **2016**, *49* (1), 244–256.
- (61) Chrissopoulou, K.; Anastasiadis, S. H. Effects of Nanoscopic-Confinement on Polymer Dynamics. *Soft Matter* **2015**, *11* (19), 3746–3766.
- (62) Larson, R. G.; Desai, P. S. Modeling the Rheology of Polymer Melts and Solutions. *Annu. Rev. Fluid Mech.* **2015**, 47 (1), 47–65.
- (63) Schneider, G. J.; Nusser, K.; Willner, L.; Falus, P.; Richter, D. Dynamics of Entangled Chains in Polymer Nanocomposites. *Macromolecules* **2011**, *44* (15), 5857–5860.
- (64) Dobkowski, Z. Determination of Critical Molecular Weight for Entangled Macromolecules Using the Tensile Strength Data. *Rheol. Acta* **1995**, 34 (6), 578–585.
- (65) Chen, J.; Li, L.; Zhou, D.; Wang, X.; Xue, G. Effect of Geometric Curvature on Vitrification Behavior for Polymer Nanotubes Confined in Anodic Aluminum Oxide Templates. *Phys. Rev. E-Stat. Nonlinear, Soft Matter Phys.* **2015**, 92 (3), 1–8.
- (66) Bansal, A.; Yang, H.; Li, C.; Cho, K.; Benicewicz, B. C.; Kumar, S. K.; Schadler, L. S. Quantitative Equivalence between Polymer Nanocomposites and Thin Polymer Films. *Nat. Mater.* **2005**, *4* (9), 693–698.
- (67) Saiter, A.; Prevosto, D.; Passaglia, E.; Couderc, H.; Delbreilh, L.; Saiter, J. M. Cooperativity Length Scale in Nanocomposites: Interfacial and Confinement Effects. *Phys. Rev. E Stat. Nonlinear, Soft Matter Phys.* **2013**, 88 (4), 1–7.
- (68) Lopez, E.; Simon, S. L. Trimerization Reaction Kinetics and Tg Depression of Polycyanurate under Nanoconfinement. *Macromolecules* **2015**, *48* (13), 4692–4701.
- (69) Park, J.-Y.; McKenna, G. Size and Confinement Effects on the Glass Transition Behavior of Polystyrene/o-Terphenyl Polymer Solutions. *Phys. Rev. B: Condens. Matter Mater. Phys.* **2000**, *61* (10), 6667–6676.
- (70) Li, L.; Chen, J.; Deng, W.; Zhang, C.; Sha, Y.; Cheng, Z.; Xue, G.; Zhou, D. Glass Transitions of Poly(Methyl Methacrylate) Confined in Nanopores: Conversion of Three- and Two-Layer Models. J. Phys. Chem. B 2015, 119 (15), 5047–5054.

(71) Zheng, X.; Rafailovich, M.; Sokolov, J.; Strzhemechny, Y.; Schwarz, S.; Sauer, B.; Rubinstein, M. Long-Range Effects on Polymer Diffusion Induced by a Bounding Interface. *Phys. Rev. Lett.* **1997**, 79 (2), 241–244.

- (72) Hartlen, K. D.; Athanasopoulos, A. P. T.; Kitaev, V. Facile Preparation of Highly Monodisperse Small Silica Spheres (15 to > 200 Nm) Suitable for Colloidal Templating and Formation of Ordered Arrays. *Langmuir* **2008**, *24* (5), 1714–1720.
- (73) Ge, D.; Yang, X.; Chen, Z.; Yang, L.; Wu, G.; Xia, Y.; Yang, S. Colloidal Inks from Bumpy Colloidal Nanoparticles for the Assembly of Ultrasmooth and Uniform Structural Colors. *Nanoscale* **2017**, *9*, 17357–17363.
- (74) Liu, T.; Cheng, K.; Salami-Ranjbaran, E.; Gao, F.; Li, C.; Tong, X.; Lin, Y.-C.; Zhang, Y.; Zhang, W.; Klinge, L.; Walsh, P. J.; Fakhraai, Z. The Effect of Chemical Structure on the Stability of Physical Vapor Deposited Glasses of 1,3,5-Triarylbenzene. *J. Chem. Phys.* **2015**, *143* (8), 084506.
- (75) Ogieglo, W.; Wormeester, H.; Wessling, M.; Benes, N. E. Spectroscopic Ellipsometry Analysis of a Thin Film Composite Membrane Consisting of Polysulfone on a Porous α -Alumina Support. ACS Appl. Mater. Interfaces 2012, 4, 935–943.
- (76) An, L.; He, D.; Jing, J.; Wang, Z.; Yu, D.; Jiang, B.; Jiang, Z.; Ma, R. Effects of Molecular Weight and Interaction Parameter on the Glass Transition Temperature of Polystyrene Mixtures and Its Blends with Polystyrene/Poly (2,6-Dimethyl-p-Phenylene Oxide). *Eur. Polym. J.* 1997, 33 (9), 1523–1528.
- (77) Papadopoulos, P.; Peristeraki, D.; Floudas, G.; Koutalas, G.; Hadjichristidis, N. Origin of Glass Transition of Poly(2-Vinylpyridine). A Temperature- and Pressure-Dependent Dielectric Spectroscopy Study. *Macromolecules* **2004**, *37* (21), 8116–8122.